Science Advances
AAAS

Supplementary Materials for

Regulation of PD-L1 through direct binding of cholesterol to CRAC motifs

Qian Wang *et al.*

Corresponding author: Shuqing Wang, wangshuqing@tmu.edu.cn; Maorong Wen, mrwen@sibcb.ac.cn;
Bo OuYang, ouyang@sibcb.ac.cn

Sci. Adv. **8**, eabq4722 (2022)
DOI: 10.1126/sciadv.abq4722

This PDF file includes:

Figs. S1 to S10
Table S1
References

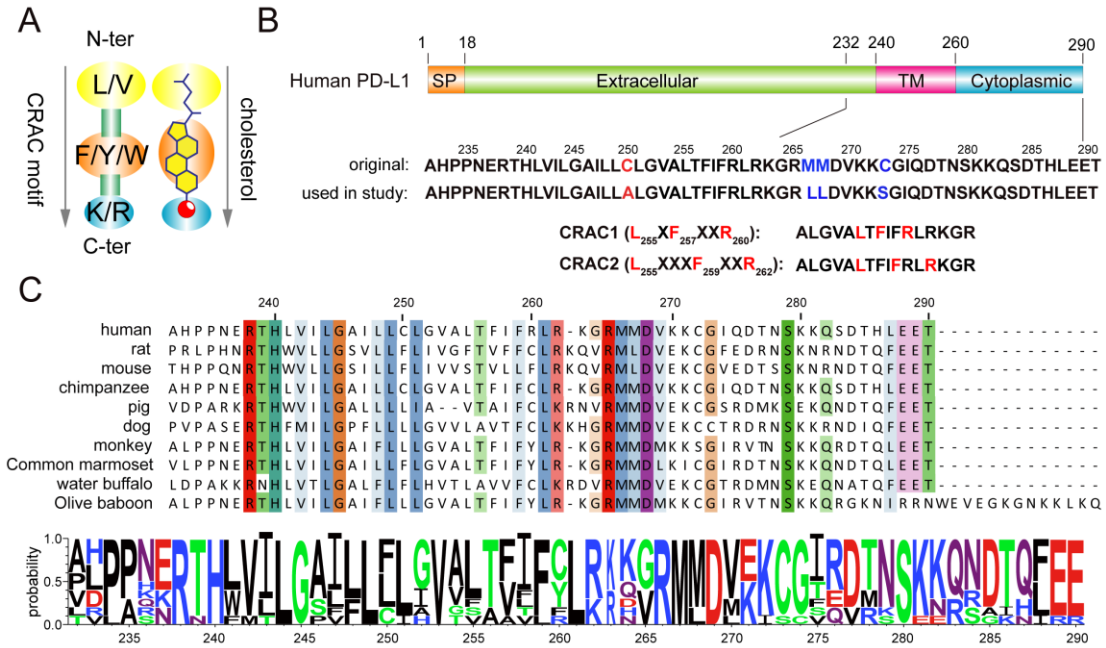

figure S1. Evolutionary conservation of key PD-L1-TC features

(A) The vectorial arrangement of the CRAC motif *(59)* is shown with the cholesterol molecule –OH group binding the K/R residues with hydrogen bonding, the cholesterol acyl tail binding the L/V residues through hydrophobic interactions, and the cholesterol rings binding the F/Y/W residues through π-π interactions.

(B) The domain organization of human PD-L1 and the amino acid sequence of PD-L1-TC (residues 232 to 290). The PD-L1-TC constructs used in this study are shown with the cysteine and methionine residues (colored in blue) mutated. Residues colored in red represent the two predicted cholesterol binding motifs: CRAC1 (containing residues L255, F257, and R260) and CRAC2 (containing residues L255, F259, and R262).

(C) Ten vertebrate species were chosen for PD-L1 protein alignment. The sequence logo *(60)* (lower panel) illustrates the degree of amino acid conservation based on PD-L1-TC alignments. The relative conservation of each amino acid residue is indicated by the height of each letter stack. Amino acids are color-coded as basic (blue), acidic (red), neutral (purple), polar (green), or hydrophobic (black). We noticed that the conserved CRAC motif in mouse shifts one residue from that of other species.

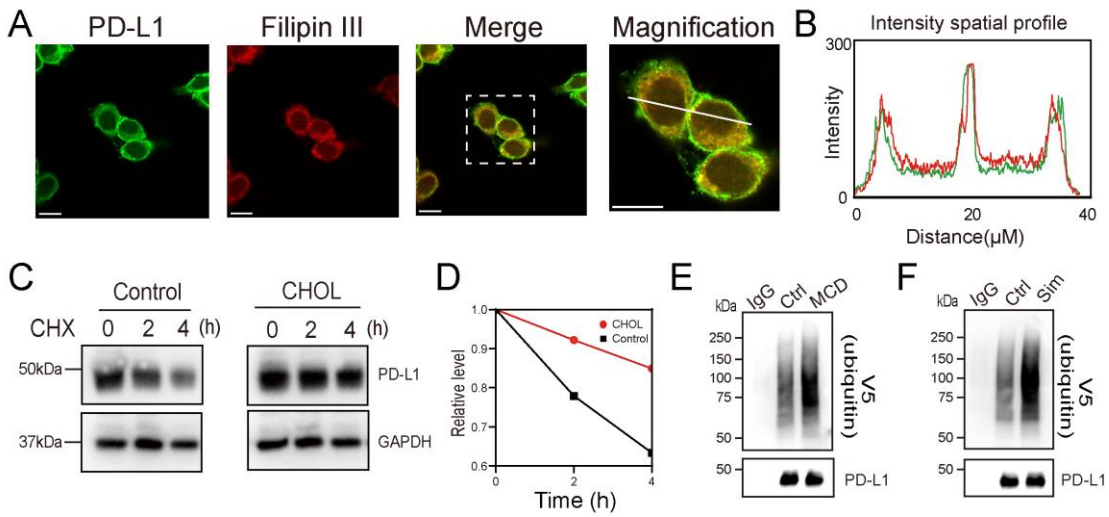

figure S2. Cholesterol colocalizes and stabilizes PD-L1 in RKO cells

(A) Representative fluorescent images demonstrating colocalization of endogenous PD-L1 and cholesterol on the plasma membranes, obtained with confocal fluorescence microscopy. RKO cells were stained with anti-PD-L1 antibody (green) and Filipin III (red). Scale bar = 15 μm. This experiment was repeated twice independently and showed similar results.

(B) Fluorescence intensity profiles of endogenous PD-L1 and Filipin III seen along the white line in the rightmost panel of (A). The intensities (y-axis) are plotted across the white line (x-axis) with the colocalizing sites indicated by yellow arrows. The data were quantified with ImageJ.

(C-D) RKO cells were incubated with cycloheximide (CHX, 50 μM) (left) or with CHX and cholesterol (20 μM) (right). PD-L1 levels were analyzed via Western blot at the indicated time points (C). The intensity of PD-L1 expression (normalized to GAPDH) was quantified with ImageJ (D). The experiment was repeated twice independently with similar results.

(E-F) The ubiquitination level of PD-L1 in HEK293FT cells was substantially increased after the addition of MCD or simvastatin. HEK293FT cells expressing exogenous V5-ubiquitin and PD-L1 were cultured with MCD (5 mM for 6 hours) (E) or simvastatin (Sim, 10 μM for 12 hours) (F). After treatment with 20 μM MG132 for an additional 4 hours, PD-L1 ubiquitination was measured with V5 immunoblotting after immunoprecipitation with anti-PD-L1 antibody; immunoglobulin G (IgG) was used as the control. This experiment was repeated twice independently with similar results.

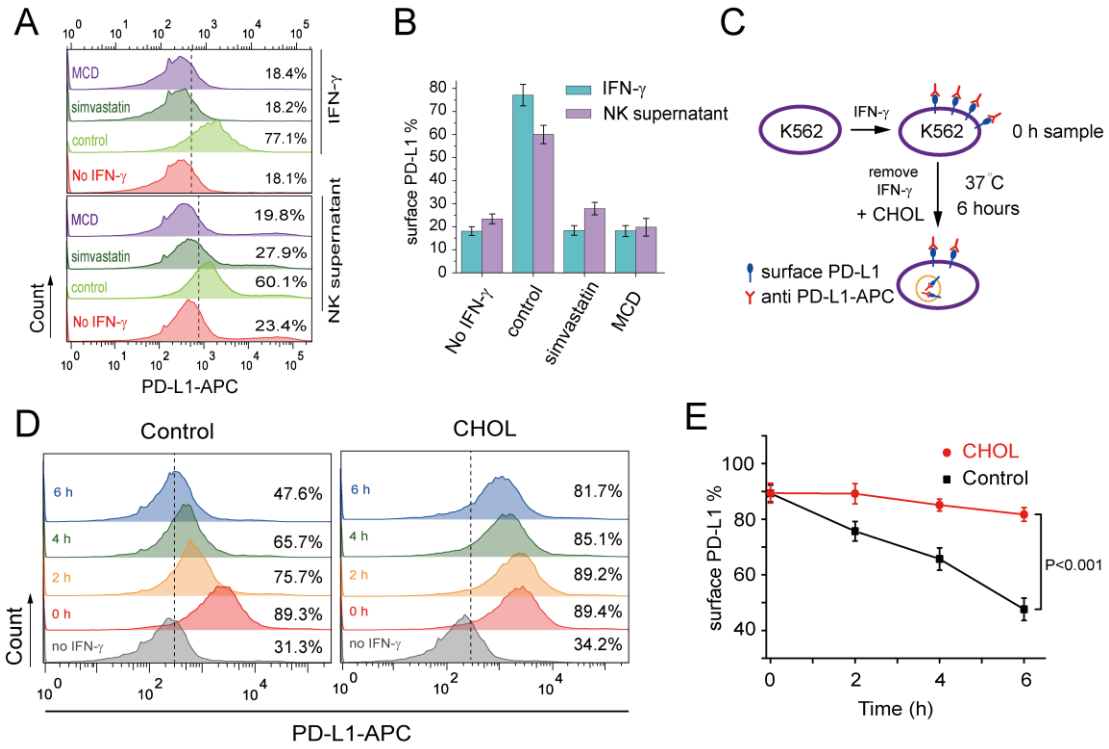

figure S3. Effects of cholesterol on cell surface PD-L1 levels of K562 cells

(A-B) Flow cytometric analysis of cell surface PD-L1 abundance in K562 cells. K562 cells were pre-treated with 50 U/ml IFN-γ (upper four curves) or NK supernatant (lower four curves) for 12 hours, then were treated with MCD (5 mM) or simvastatin (10 μM) (A). Levels of PD-L1 were quantified with ImageJ (B).

(C) Diagram showing the assay performed to study changes in the levels of PD-L1 on K562 cell surfaces after control or cholesterol treatment. K562 cells were pre-treated with 50 U/ml IFN-γ for 12 hours, then cell surface PD-L1 was labelled with anti-PD-L1 antibody at 4 °C. After washing off unbound antibody, cells were incubated at 37 °C with or without cholesterol. PD-L1 levels were then recorded at 0, 2, 4, and 6 hours via flow cytometric analysis.

(D-E) Following the procedure shown in (C), levels of PD-L1 on the surface of K562 cells were analyzed by flow cytometry in the absence (left) or presence (right) of 25 μM cholesterol at the indicated time points (D). Relative abundance of membrane PD-L1 was quantified with FlowJo (E).

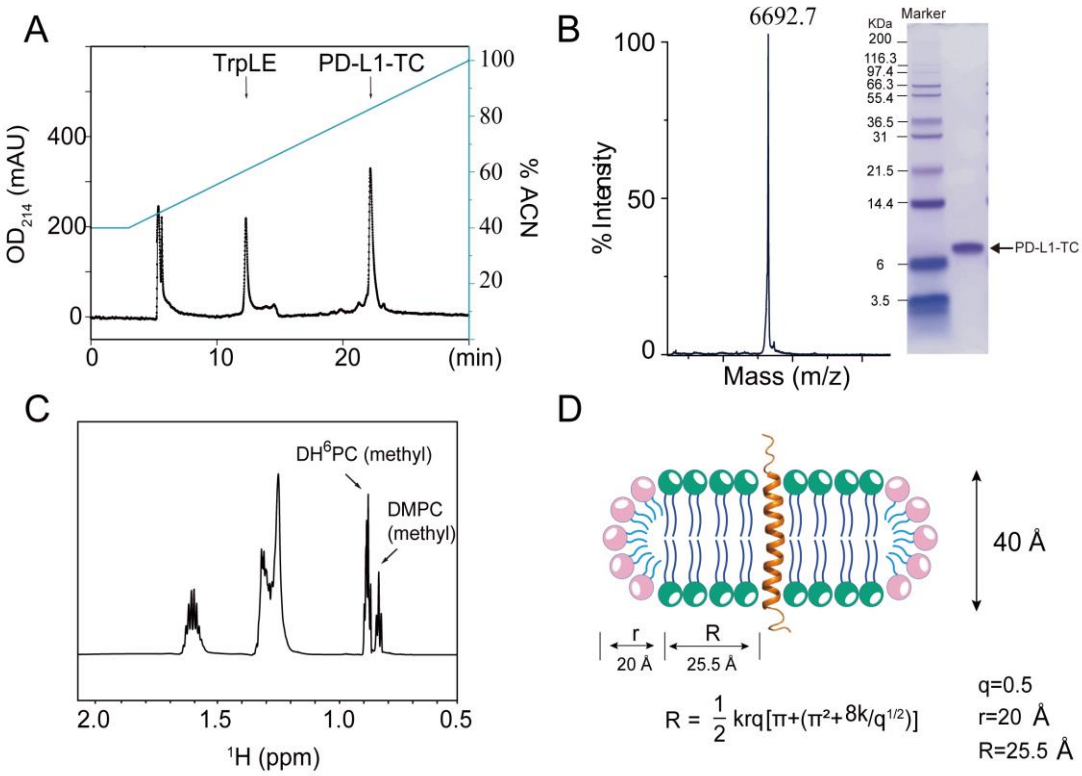

figure S4. Expression, purification, and bicelle reconstitution of PD-L1-TC

(A) Reverse phase HPLC purification of human PD-L1-TC from CNBr-cleaved TrpLE-PD-L1-TC on a Zorbax SB-C3 column with a gradient from 40-100% acetonitrile (ACN) and 0.1% trifluoroacetic acid (TFA). The purified PD-L1-TC product was verified with SDS-PAGE and mass spectrometry.

(B) MALDI-TOF mass spectrometry signal (left) and SDS-PAGE results (right) showing HPLC-purified PD-L1-TC protein. The molecular weight (MW) of PD-L1-TC was measured as 6692.7 Da; the theoretical MW of the monomer is 6683.71 Da.

(C) ^{1}H NMR spectrum of the DH^{6}PC and DMPC methyl peaks from PD-L1-TC NMR sample. The bicelle q value calculated using the integrated areas of the DH^{6}PC and DMPC methyl peaks was 0.5.

(D) Schematic illustration of PD-L1-TC reconstituted in DMPC/DH^{6}PC bicelles with the planar lipid bilayer formed by DMPC in a radius of 25.5 Å and the micellar lipid rim formed by DH^{6}PC in a radius of 20 Å.

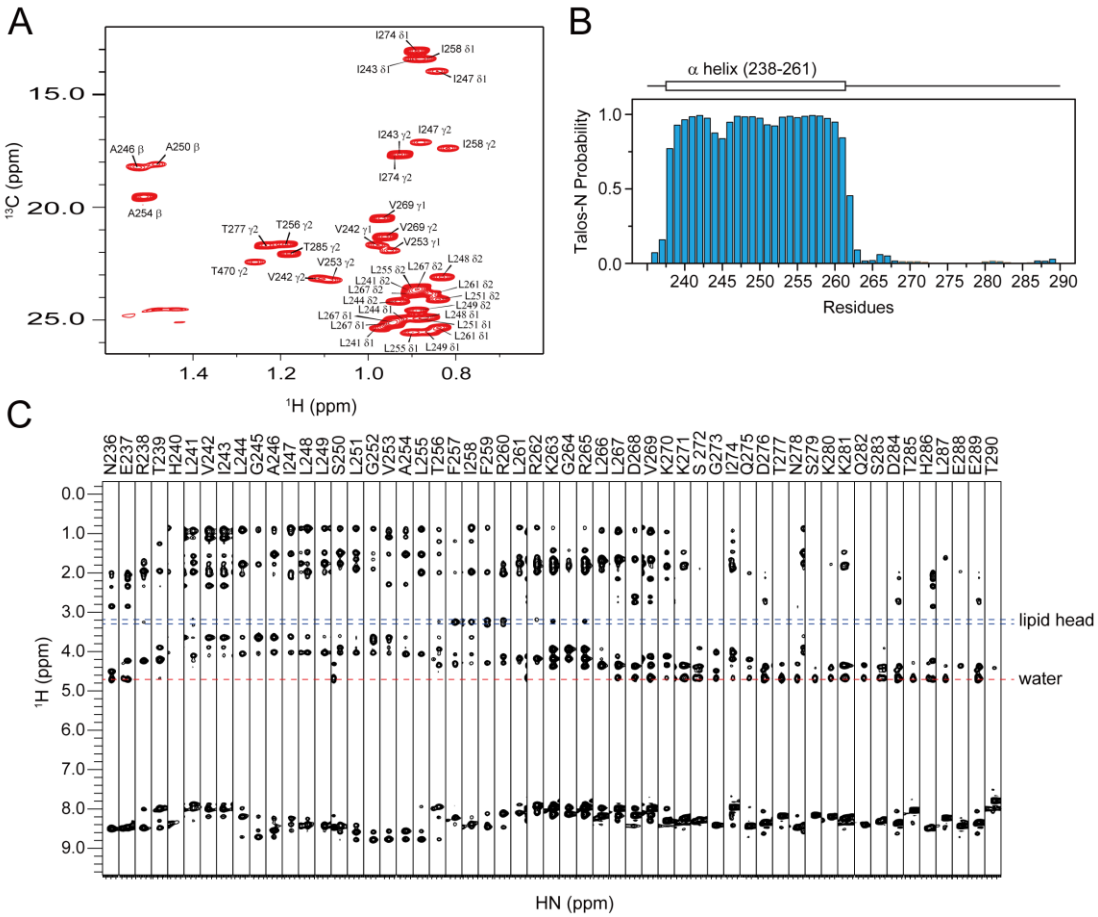

figure S5. NMR characterization of PD-L1-TC in bicelles

(A) The methyl group region of the 2D ^{1}H,^{13}C HSQC with 28 ms constant-time ^{13}C evolution, recorded at an ^{1}H frequency of 900 MHz, using (^{15}N, ^{13}C)-labeled PD-L1-TC protein.

(B) Chemical-shift-based secondary structure prediction of PD-L1-TC in bicelles. The graph shows the probability of each residue being part of the α helix, as determined with TALOS+ software *(31)*.

(C) Residue-specific strips taken from the 3D ^{15}N-separated NOESY-TROSY-HSQC spectrum (NOE mixing time = 120 ms) recorded at 900 MHz using the (^{15}N, ^{13}C)-labeled PD-L1-TC in deuterated DMPC/DH^{6}PC bicelles. Water peaks are indicated by the red dotted line.

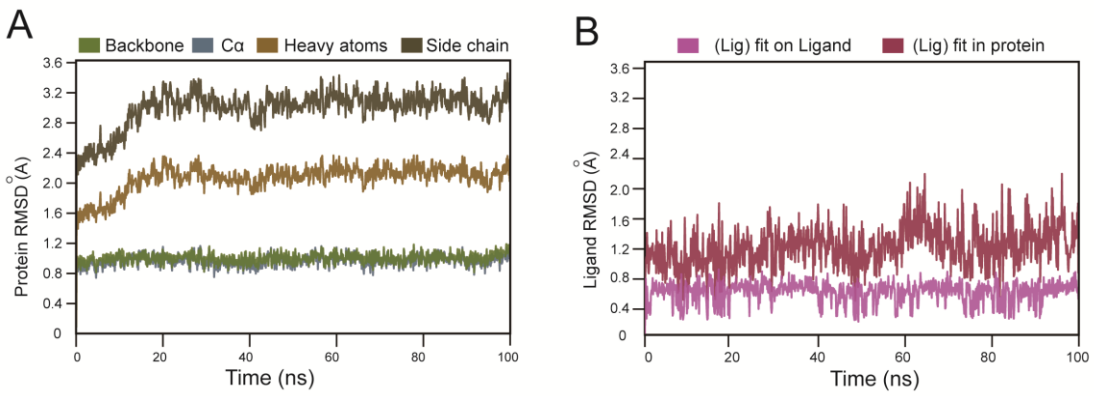

figure S6. MD simulation of PD-L1 with cholesterol

(A) Root-mean-square deviation (RMSD) plots of a selection of atoms in the PD-L1 protein against simulation time, showing system convergence and stability of simulations. Green lines: backbone atoms; Blue lines: Cα atoms; brown lines: heavy atoms; dark brown lines: sidechain atoms.

(B) RMSD plots of cholesterol against simulation time, showing system convergence and stability of simulations. Purple lines: ligand atoms fitting on ligand; dark red lines: cholesterol atoms fitting on PD-L1 protein.

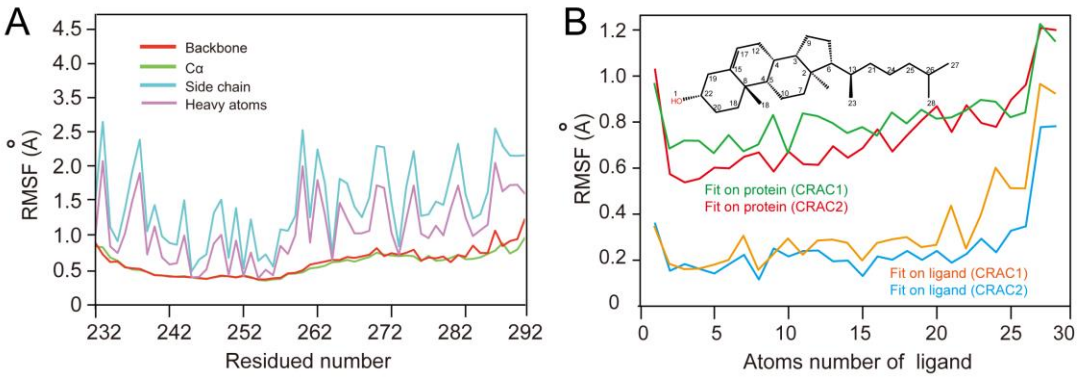

figure S7. MD simulation of PD-L1 with cholesterol

(A) Root mean square fluctuation (RMSF) was used to characterize local changes along the protein chain. Peaks indicate areas of the protein that fluctuated the most during the simulation. Overall, the protein backbone atoms were highly stable, with RMSF values below 1 Å when cholesterol binds to CRAC1 or CRAC2 motif. Typically the tails (N- and C-terminal) fluctuate more than any other part of the protein. Secondary structure elements such as α-helices in the membrane (residues 240 to 262) are usually more stable than the unstructured part of the protein, and thus fluctuate less than the loop regions.

(B) RMSF was calculated for the ligand, which may provide insights into how ligand fragments interact with the protein during the binding event, after energy minimization. The RMSF values of cholesterol atoms were smaller than 1 Å, indicating that the ligand is stable with respect to the protein. However, the rigid part (four rings) of cholesterol is more stable than the tail region, meaning that the rigid segment is the primary region of interaction with the protein.

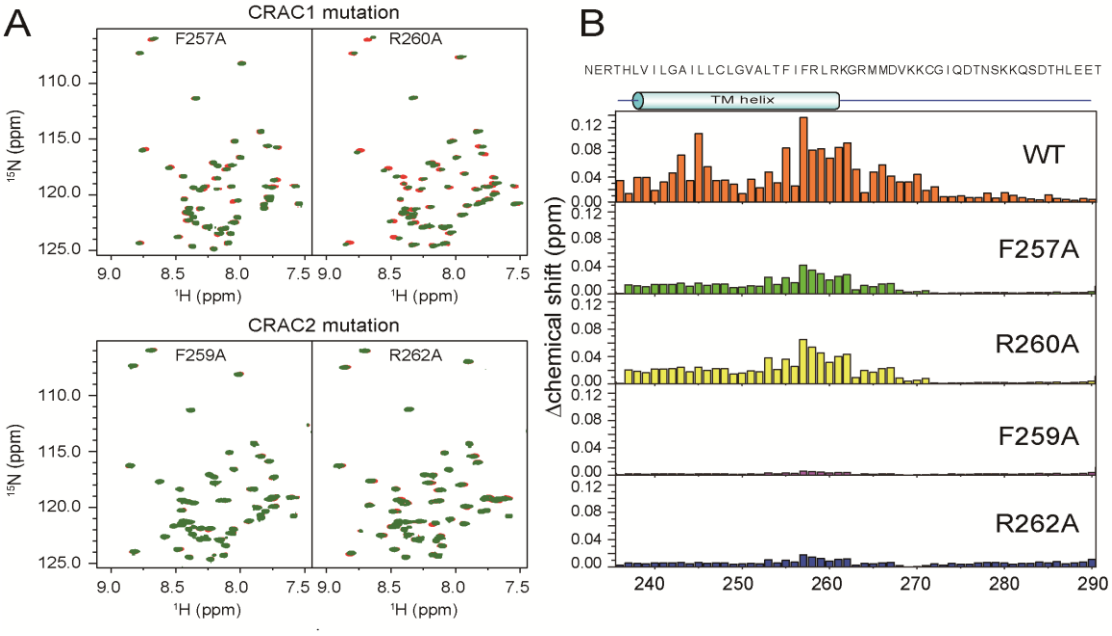

figure S8. Cholesterol binding sites verified by NMR titrations with mutant proteins
(A) ^{1}H-^{15}N TROSY-HSQC spectra of the mutant proteins PD-L1-TC^{F257A}, PD-L1-TC^{F259A}, PD-L1-TC^{R260A}, and PD-L1-TC^{R262A} in the absence (red) or presence (green) of 1.5 mM cholesterol. (B) Comparison of NMR chemical shift changes for PD-L1-TC^{WT} and PD-L1-TC mutants in the absence and presence of 1.5 mM cholesterol in DMPC/DH^{6}PC bicelles.

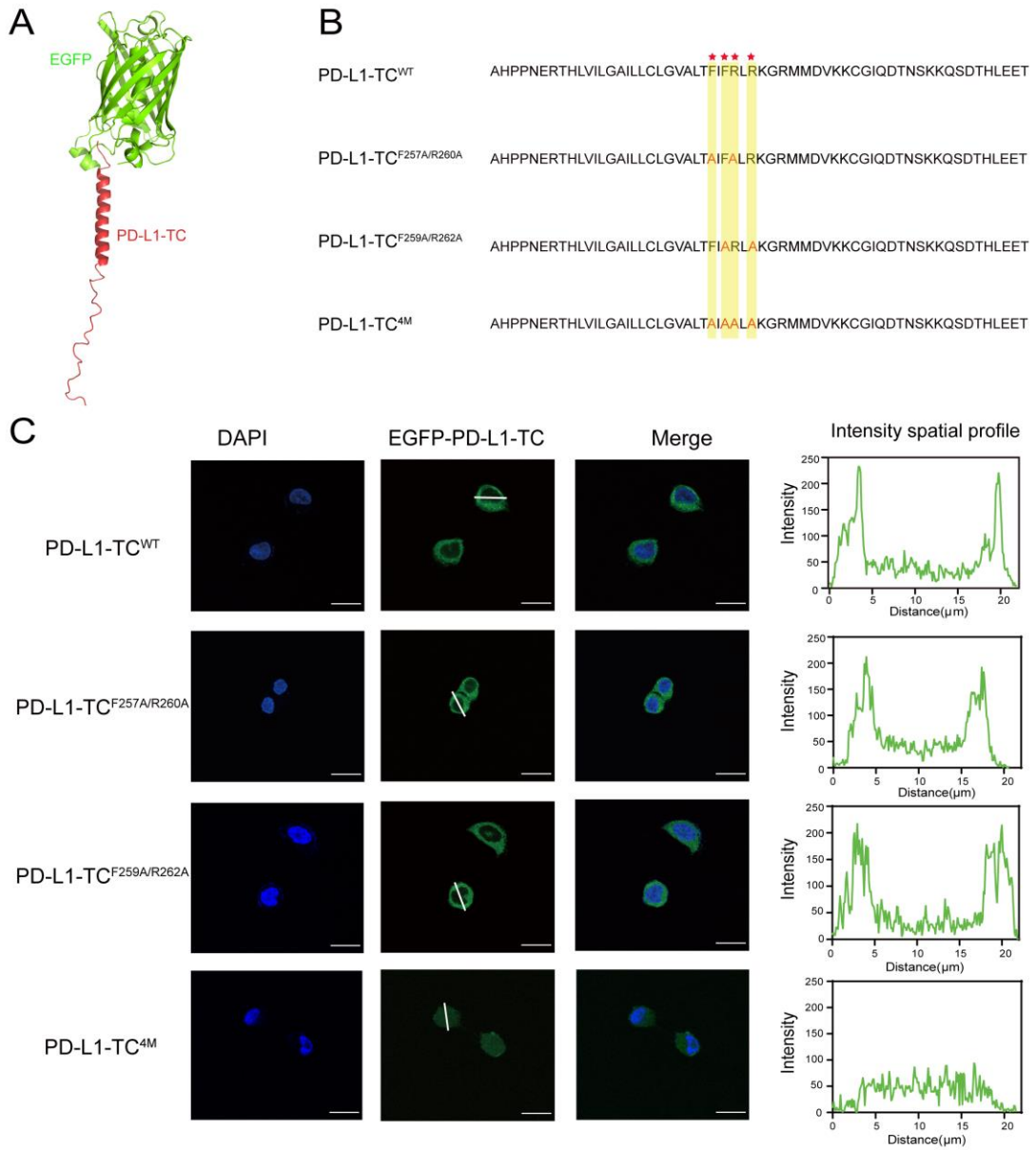

figure S9. CRAC motifs are critical for localization of PD-L1

(A) Schematic illustration of the EGFP-PD-L1-TC fusion protein, including EGFP (green) and PD-L1-TC (residues 232 to 290, magenta).

(B) Amino acid sequences of PD-L1-TC^{WT}, PD-L1-TC$^{F257A/R260A}$, PD-L1-TC$^{F259A/R262A}$, and PD-L1-TC^{4M}.

(C) RKO cells were transfected with EGFP-PD-L1-TC^{WT}, EGFP-PD-L1-TC$^{F257A/R260A}$, EGFP-PD-L1-TC$^{F259A/R262A}$, or EGFP-PD-L1-TC^{4M} plasmid and observed with confocal microscopy. Scale bars = 20 μm. The intensity profiles of PD-L1 as indicated with white lines are plotted at right. The assay was repeated twice with similar results.

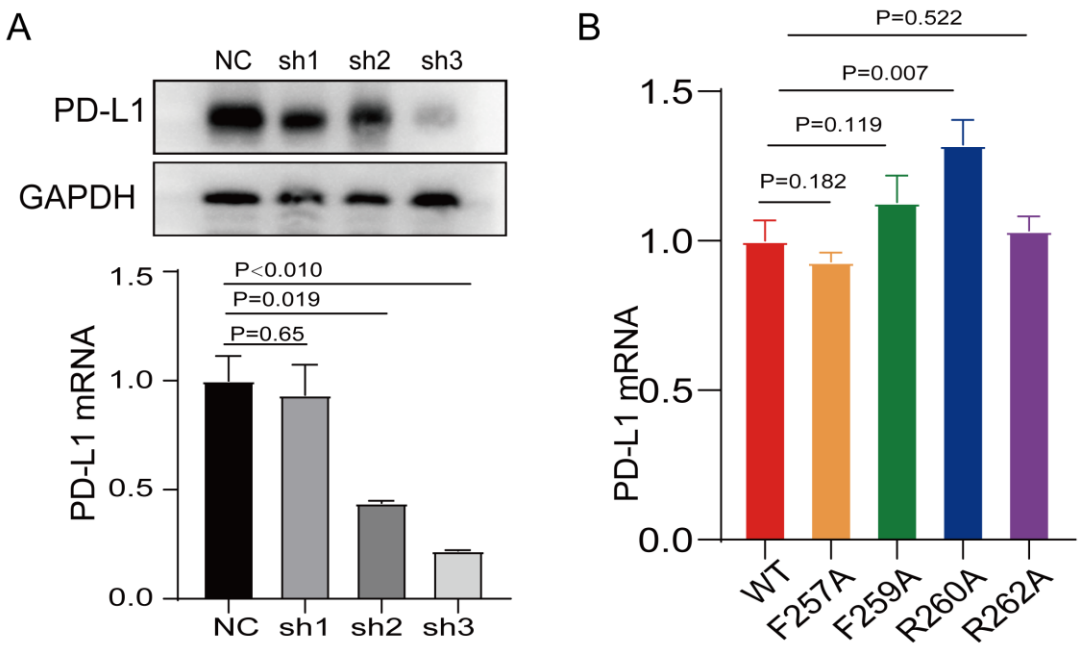

figure S10. Detection of PD-L1 protein and mRNA levels in PD-L1-knockdown RKO cells

(A) The knockdown effect on endogenous PD-L1 in RKO cells was analyzed by Western blot (upper panel) and RT-qPCR (lower panel). Data are shown as the means ± SD (n = 3). *P* values were calculated with unpaired two-sided Student's *t*-test. NC indicates the negative control using non-targeting shRNA; sh1–sh3 are the PD-L1 knockdown cell lines, which used different targeting shRNAs as described in the Methods.

(B) mRNA levels of PD-L1 in endogenous PD-L1-knockdown RKO stable cells expressing exogenous PD-L1-TC^{WT}, PD-L1-TC^{F257A}, PD-L1-TC^{F259A}, PD-L1-TC^{R260A}, or PD-L1-TC^{R262A} were analyzed by RT-qPCR. Data are shown as the means ± SD (n = 2). *P* values were calculated with unpaired two-sided Student's *t*-test.

table S1. NMR and Refinement Statistics for PD-L1-TC Structures (PDB 7DCV)

NMR Distance and Dihedral Constraints	
Distance constraints from NOE	330
Intra-chain NOEs	278
Inter-residue	240
Sequential (|i – j| = 1)	140
Medium-range (1< |i – j| < 4)	52
Long-range (|i–j| ≥ 4)	48
Hydrogen bonds	38
Total dihedral angle restraints	52
ϕ (TALOS)	26
Ψ (TALOS)	26
Structure Statistics [a]	
Violations (means ± SD)	
Distance constraints (Å) Statistics	0.068 ± 0.006
Dihedral angle constraints (°)	0.036 ± 0.044
Deviations from idealized geometry	
Bond lengths (Å)	0.006 ± 0.000
Bond angles (°)	0.579 ± 0.018
Impropers (°)	0.337 ± 0.058
Average pairwise RMSD (Å) [b]	
Heavy	1.194
Backbone	0.619
Ramachandran plot statistics from psvs * (%)	
Residues in most favored regions	78.7
Residues in additional allowed regions	21.3
Residues in generously allowed regions	0.0
Residues in disallowed regions	0.0

[a] Statistics were calculated and averaged over an ensemble of the 15 lowest energy structures of the 200 calculated structures.

[b] The precision of the atomic coordinates is defined as the average RMSD between the 15 final structures and their mean coordinates. The calculation only includes the structured regions of the protein: residues 236 to 260 for PD-L1-TC.

REFERENCES AND NOTES

1. W. K. Subczynski, M. Pasenkiewicz-Gierula, J. Widomska, L. Mainali, M. Raguz, High cholesterol/low cholesterol: Effects in biological membranes: A review. *Cell Biochem. Biophys.* **75**, 369–385 (2017).

2. P. L. Yeagle, Non-covalent binding of membrane lipids to membrane proteins. *Biochim. Biophys. Acta* **1838**, 1548–1559 (2014).

3. J. Hu, Z. Zhang, W. J. Shen, S. Azhar, Cellular cholesterol delivery, intracellular processing and utilization for biosynthesis of steroid hormones. *Nutr. Metab.* **7**, 47 (2010).

4. J. Grouleff, S. J. Irudayam, K. K. Skeby, B. Schiott, The influence of cholesterol on membrane protein structure, function, and dynamics studied by molecular dynamics simulations. *Biochim. Biophys. Acta* **1848**, 1783–1795 (2015).

5. Y. Song, A. K. Kenworthy, C. R. Sanders, Cholesterol as a co-solvent and a ligand for membrane proteins. *Protein Sci.* **23**, 1–22 (2014).

6. B. P. Weiser, R. Salari, R. G. Eckenhoff, G. Brannigan, Computational investigation of cholesterol binding sites on mitochondrial VDAC. *J. Phys. Chem. B* **118**, 9852–9860 (2014).

7. V. Cherezov, D. M. Rosenbaum, M. A. Hanson, S. G. Rasmussen, F. S. Thian, T. S. Kobilka, H. J. Choi, P. Kuhn, W. I. Weis, B. K. Kobilka, R. C. Stevens, High-resolution crystal structure of an engineered human β_2-adrenergic G protein–coupled receptor. *Science* **318**, 1258–1265 (2007).

8. W. Liu, E. Chun, A. A. Thompson, P. Chubukov, F. Xu, V. Katritch, G. W. Han, C. B. Roth, L. H. Heitman, A. P. IJzerman, V. Cherezov, R. C. Stevens, Structural basis for allosteric regulation of GPCRs by sodium ions. *Science* **337**, 232–236 (2012).

9. M. Zocher, C. Zhang, S. G. Rasmussen, B. K. Kobilka, D. J. Muller, Cholesterol increases kinetic, energetic, and mechanical stability of the human β_2-adrenergic receptor. *Proc. Natl. Acad. Sci. U.S.A.* **109**, E3463–E3472 (2012).

10. B. I. Sejdiu, D. P. Tieleman, Lipid-protein interactions are a unique property and defining feature of G protein-coupled receptors. *Biophys. J.* **118**, 1887–1900 (2020).

11. S. Gahbauer, R. A. Bockmann, Membrane-mediated oligomerization of G protein coupled receptors and its implications for GPCR function. *Front. Physiol.* **7**, 494 (2016).

12. D. H. Nguyen, D. Taub, CXCR4 function requires membrane cholesterol: Implications for HIV infection. *J. Immunol.* **168**, 4121–4126 (2002).

13. N. Jamin, J. M. Neumann, M. A. Ostuni, T. K. Vu, Z.-X. Yao, S. Murail, J.-C. Robert, C. Giatzakis, V. Papadopoulos, J.-J. Lacapère, Characterization of the cholesterol recognition amino acid consensus sequence of the peripheral-type benzodiazepine receptor. *Mol. Endocrinol.* **19**, 588–594 (2005).

14. H. Li, V. Papadopoulos, Peripheral-type benzodiazepine receptor function in cholesterol transport. Identification of a putative cholesterol recognition/interaction amino acid sequence and consensus pattern. *Endocrinology* **139**, 4991–4997 (1998).

15. C. J. Baier, J. Fantini, F. J. Barrantes, Disclosure of cholesterol recognition motifs in transmembrane domains of the human nicotinic acetylcholine receptor. *Sci. Rep.* **1**, 69 (2011).

16. M. A. Hanson, V. Cherezov, M. T. Griffith, C. B. Roth, V. P. Jaakola, E. Y. Chien, J. Velasquez, P. Kuhn, R. C. Stevens, A specific cholesterol binding site is established by the 2.8 A structure of the human β_2-adrenergic receptor. *Structure* **16**, 897–905 (2008).

17. B. Huang, B. L. Song, C. Xu, Cholesterol metabolism in cancer: Mechanisms and therapeutic opportunities. *Nat. Metab.* **2**, 132–141 (2020).

18. H. Xu, S. Zhou, Q. Tang, H. Xia, F. Bi, Cholesterol metabolism: New functions and therapeutic approaches in cancer. *Biochim. Biophys. Acta Rev. Cancer* **1874**, 188394 (2020).

19. W. Liu, B. Chakraborty, R. Safi, D. Kazmin, C. Y. Chang, D. P. McDonnell, Dysregulated cholesterol homeostasis results in resistance to ferroptosis increasing tumorigenicity and metastasis in cancer. *Nat. Commun.* **12**, 5103 (2021).

20. E. Di Bello, C. Zwergel, A. Mai, S. Valente, The innovative potential of statins in cancer: New targets for new therapies. *Front. Chem.* **8**, 516 (2020).

21. X. Ma, E. Bi, Y. Lu, P. Su, C. Huang, L. Liu, Q. Wang, M. Yang, M. F. Kalady, J. Qian, A. Zhang, A. A. Gupte, D. J. Hamilton, C. Zheng, Q. Yi, Cholesterol induces $CD8^+$ T cell exhaustion in the tumor microenvironment. *Cell Metab.* **30**, 143–156.e5 (2019).

22. W. Yang, Y. Bai, Y. Xiong, J. Zhang, S. Chen, X. Zheng, X. Meng, L. Li, J. Wang, C. Xu, C. Yan, L. Wang, C. C. Chang, T.-Y. Chang, T. Zhang, P. Zhou, B.-L. Song, W. Liu, S.-c. Sun, X. Liu, B.-l. Li, C. Xu, Potentiating the antitumour response of $CD8^+$ T cells by modulating cholesterol metabolism. *Nature* **531**, 651–655 (2016).

23. Y. Shi, Regulatory mechanisms of PD-L1 expression in cancer cells. *Cancer Immunol. Immunother.* **67**, 1481–1489 (2018).

24. V. Zinchuk, O. Zinchuk, Quantitative colocalization analysis of confocal fluorescence microscopy images. *Curr. Protoc. Cell Biol.* **Chapter 4**, Unit 4.19 (2008).

25. H. Wang, H. Yao, C. Li, H. Shi, J. Lan, Z. Li, Y. Zhang, L. Liang, J. Y. Fang, J. Xu, HIP1R targets PD-L1 to lysosomal degradation to alter T cell-mediated cytotoxicity. *Nat. Chem. Biol.* **15**, 42–50 (2019).

26. N. Mohammad, P. Malvi, A. S. Meena, S. V. Singh, B. Chaube, G. Vannuruswamy, M. J. Kulkarni, M. K. Bhat, Cholesterol depletion by methyl-β-cyclodextrin augments tamoxifen induced cell death by enhancing its uptake in melanoma. *Mol. Cancer* **13**, 204 (2014).

27. A. Branchi, A. M. Fiorenza, A. Torri, F. Muzio, C. Berra, E. Colombo, E. Dalla Valle, A. Rovellini, D. Sommariva, Effects of low doses of simvastatin and atorvastatin on high-density lipoprotein cholesterol levels in patients with hypercholesterolemia. *Clin. Ther.* **23**, 851–857 (2001).

28. R. Bellucci, A. Martin, D. Bommarito, K. Wang, S. H. Hansen, G. J. Freeman, J. Ritz, Interferon-γ-induced activation of JAK1 and JAK2 suppresses tumor cell susceptibility to NK cells through upregulation of PD-L1 expression. *Onco. Targets. Ther.* **4**, e1008824 (2015).

29. Q. Fu, A. Piai, W. Chen, K. Xia, J. J. Chou, Structure determination protocol for transmembrane domain oligomers. *Nat. Protoc.* **14**, 2483–2520 (2019).

30. M. Salzmann, K. Pervushin, G. Wider, H. Senn, K. Wuthrich, TROSY in triple-resonance experiments: New perspectives for sequential NMR assignment of large proteins. *Proc. Natl. Acad. Sci. U.S.A.* **95**, 13585–13590 (1998).

31. Y. Shen, F. Delaglio, G. Cornilescu, A. Bax, TALOS^{+}: A hybrid method for predicting protein backbone torsion angles from NMR chemical shifts. *J. Biomol. NMR* **44**, 213–223 (2009).

32. A. Piai, Q. Fu, J. Dev, J. J. Chou, Optimal bicelle size q for solution NMR studies of the protein transmembrane partition. *Chemistry* **23**, 1361–1367 (2017).

33. H. Wu, R. Cao, S. Wei, S. Pathan-Chhatbar, M. Wen, B. Wu, W. W. Schamel, S. Wang, B. OuYang, Cholesterol binds in a reversed orientation to TCRβ-TM in which its OH group is localized to the center of the lipid bilayer. *J. Mol. Biol.* **433**, 167328 (2021).

34. J. N. Weiss, The Hill equation revisited: Uses and misuses. *FASEB J.* **11**, 835–841 (1997).

35. J. Eberhardt, D. Santos-Martins, A. F. Tillack, S. Forli, AutoDock vina 1.2.0: New docking methods, expanded force field, and Python bindings. *J. Chem. Inf. Model* **61**, 3891–3898 (2021).

36. G. Jaipuria, A. Leonov, K. Giller, S. K. Vasa, L. Jaremko, M. Jaremko, R. Linser, S. Becker, M. Zweckstetter, Cholesterol-mediated allosteric regulation of the mitochondrial translocator protein structure. *Nat. Commun.* **8**, 14893 (2017).

37. M. R. Elkins, J. K. Williams, M. D. Gelenter, P. Dai, B. Kwon, I. V. Sergeyev, B. L. Pentelute, M. Hong, Cholesterol-binding site of the influenza M2 protein in lipid bilayers from solid-state NMR. *Proc. Natl. Acad. Sci. U.S.A.* **114**, 12946–12951 (2017).

38. M. Wen, Y. Cao, B. Wu, T. Xiao, R. Cao, Q. Wang, X. Liu, H. Xue, Y. Yu, J. Lin, C. Xu, J. Xu, B. OuYang, PD-L1 degradation is regulated by electrostatic membrane association of its cytoplasmic domain. *Nat. Commun.* **12**, 5106 (2021).

39. J. Zhang, X. Bu, H. Wang, Y. Zhu, Y. Geng, N. T. Nihira, Y. Tan, Y. Ci, F. Wu, X. Dai, J. Guo, Y. H. Huang, C. Fan, S. Ren, Y. Sun, G. J. Freeman, P. Sicinski, W. Wei, Cyclin D-CDK4 kinase destabilizes PD-L1 via cullin 3-SPOP to control cancer immune surveillance. *Nature* **553**, 91–95 (2018).

40. H. Yao, J. Lan, C. Li, H. Shi, J. P. Brosseau, H. Wang, H. Lu, C. Fang, Y. Zhang, L. Liang, X. Zhou, C. Wang, Y. Xue, Y. Cui, J. Xu, Inhibiting PD-L1 palmitoylation enhances T-cell immune responses against tumours. *Nat. Biomed. Eng.* **3**, 306–317 (2019).

41. W. J. Lim, M. Lee, Y. Oh, X. Q. Fang, S. Lee, C. H. Lim, J. Park, J. H. Lim, Statins decrease programmed death-ligand 1 (PD-L1) by inhibiting AKT and beta-catenin signaling. *Cells* **10,** 2488 (2021).

42. W. Ni, H. Mo, Y. Liu, Y. Xu, C. Qin, Y. Zhou, Y. Li, Y. Li, A. Zhou, S. Yao, R. Zhou, J. Huo, L. Che, J. Li, Targeting cholesterol biosynthesis promotes anti-tumor immunity by inhibiting long noncoding RNA SNHG29-mediated YAP activation. *Mol. Ther.* **29**, 2995–3010 (2021).

43. E. B. Garon, N. A. Rizvi, R. Hui, N. Leighl, A. S. Balmanoukian, J. P. Eder, A. Patnaik, C. Aggarwal, M. Gubens, L. Horn, E. Carcereny, M. J. Ahn, E. Felip, J. S. Lee, M. D. Hellmann, O. Hamid, J. W. Goldman, J. C. Soria, M. Dolled-Filhart, R. Z. Rutledge, J. Zhang, J. K. Lunceford, R. Rangwala, G. M. Lubiniecki, C. Roach, K. Emancipator, L. Gandhi; KEYNOTE-001 Investigators, Pembrolizumab for the treatment of non-small-cell lung cancer. *N. Engl. J. Med.* **372**, 2018–2028 (2015).

44. J. Brahmer, K. L. Reckamp, P. Baas, L. Crino, W. E. Eberhardt, E. Poddubskaya, S. Antonia, A. Pluzanski, E. E. Vokes, E. Holgado, D. Waterhouse, N. Ready, J. Gainor, O. Aren Frontera, L. Havel, M. Steins, M. C. Garassino, J. G. Aerts, M. Domine, L. Paz-Ares, M. Reck, C. Baudelet, C. T. Harbison, B. Lestini, D. R. Spigel, Nivolumab versus docetaxel in advanced squamous-cell non-small-cell lung cancer. *N. Engl. J. Med.* **373**, 123–135 (2015).

45. T. S. Nowicki, S. Hu-Lieskovan, A. Ribas, Mechanisms of resistance to PD-1 and PD-L1 blockade. *Cancer J.* **24**, 47–53 (2018).

46. Q. Wu, L. Jiang, S. C. Li, Q. J. He, B. Yang, J. Cao, Small molecule inhibitors targeting the PD-1/PD-L1 signaling pathway. *Acta Pharmacol. Sin.* **42**, 1–9 (2021).

47. F. Delaglio, S. Grzesiek, G. W. Vuister, G. Zhu, J. Pfeifer, A. Bax, NMRPipe: A multidimensional spectral processing system based on UNIX pipes. *J. Biomol. NMR* **6**, 277–293 (1995).

48. C. Bartels, T. H. Xia, M. Billeter, P. Güntert, K. Wüthrich, The program XEASY for computer-supported NMR spectral analysis of biological macromolecules. *J. Biomol. NMR* **6**, 1–10 (1995).

49. Y. Xia, K. Sze, G. Zhu, Transverse relaxation optimized 3D and 4D 15n/15N separated NOESY experiments of 15N labeled proteins. *J. Biomol. NMR* **18**, 261–268 (2000).

50. C. D. Schwieters, J. J. Kuszewski, N. Tjandra, G. M. Clore, The Xplor-NIH NMR molecular structure determination package. *J. Magn. Reson.* **160**, 65–73 (2003).

51. B. OuYang, S. Xie, M. J. Berardi, X. Zhao, J. Dev, W. Yu, B. Sun, J. J. Chou, Unusual architecture of the p7 channel from hepatitis C virus. *Nature* **498**, 521–525 (2013).

52. W. F. Vranken, W. Boucher, T. J. Stevens, R. H. Fogh, A. Pajon, M. Llinas, E. L. Ulrich, J. L. Markley, J. Ionides, E. D. Laue, The CCPN data model for NMR spectroscopy: Development of a software pipeline. *Proteins* **59**, 687–696 (2005).

53. K. J. Livak, T. D. Schmittgen, Analysis of relative gene expression data using real-time quantitative PCR and the $2^{-\Delta\Delta C_T}$ method. *Methods* **25**, 402–408 (2001).

54. C. A. Schneider, W. S. Rasband, K. W. Eliceiri, NIH Image to ImageJ: 25 years of image analysis. *Nat. Methods* **9**, 671–675 (2012).

55. W. L. Jorgensen, J. Tirado-Rives, The OPLS [optimized potentials for liquid simulations] potential functions for proteins, energy minimizations for crystals of cyclic peptides and crambin. *J. Am. Chem. Soc.* **110**, 1657–1666 (1988).

56. W. G. Hoover, Canonical dynamics: Equilibrium phase-space distributions. *Phys. Rev. A Gen. Phys.* **31**, 1695–1697 (1985).

57. Z. Deng, G. J. Martyna, M. L. Klein, Structure and dynamics of bipolarons in liquid ammonia. *Phys. Rev. Lett.* **68**, 2496–2499 (1992).

58. H. G. Petersen, Accuracy and efficiency of the particle mesh Ewald method. *J. Chem. Phys.* **103**, 3668–3679 (1995).

59. J. Fantini, R. M. Epand, F. J. Barrantes, Cholesterol-recognition motifs in membrane proteins. *Adv. Exp. Med. Biol.* **1135**, 3–25 (2019).

60. G. E. Crooks, G. Hon, J. M. Chandonia, S. E. Brenner, WebLogo: A sequence logo generator. *Genome Res.* **14**, 1188–1190 (2004).